

Low dust mass and high star-formation efficiency at $z > 12$ from deep ALMA observations

IKKI MITSUHASHI,^{1,2,3} JORGE A. ZAVALA,³ TOM J.L.C. BAKX,⁴ AKIO K. INOUE,^{2,5} MARCO CASTELLANO,⁶
ANTONELLO CALABRO,⁶ CAITLIN M. CASEY,⁷ MAXIMILIEN FRANCO,⁷ BUNYO HATSUKADE,^{3,8,9} NIMISH P. HATHI,¹⁰
RYOTA IKEDA,^{3,11} ANTON M. KOEKEMOER,¹⁰ JEYHAN KARTALTEPE,¹² KIRSTEN K. KNUDSEN,¹³ PAOLA SANTINI,⁶
TOSHIKI SAITO,¹⁴ ELENA TERLEVICH,^{15,16,17} AND ROBERTO TERLEVICH^{15,16,17}

¹*Department for Astrophysical & Planetary Science, University of Colorado, Boulder, CO 80309, USA*

²*Waseda Research Institute for Science and Engineering, Faculty of Science and Engineering, Waseda University, 3-4-1 Okubo, Shinjuku, Tokyo 169-8555, Japan*

³*National Astronomical Observatory of Japan, 2-21-1 Osawa, Mitaka, Tokyo 181-8588, Japan*

⁴*Department of Space, Earth and Environment, Chalmers University of Technology, Gothenburg, Sweden*

⁵*Department of Physics, School of Advanced Science and Engineering, Faculty of Science and Engineering, Waseda University, 3-4-1, Okubo, Shinjuku, Tokyo 169-8555, Japan*

⁶*INAF - Osservatorio Astronomico di Roma, via di Frascati 33, 00078 Monte Porzio Catone, Italy*

⁷*Department of Astronomy, The University of Texas at Austin, 2515 Speedway Boulevard Stop C1400, Austin, TX 78712, USA*

⁸*Graduate Institute for Advanced Studies, SOKENDAI, Osawa, Mitaka, Tokyo 181-8588, Japan*

⁹*Institute of Astronomy, Graduate School of Science, The University of Tokyo, 2-21-1 Osawa, Mitaka, Tokyo 181-0015, Japan*

¹⁰*Space Telescope Science Institute, 3700 San Martin Drive, Baltimore, MD 21218, USA*

¹¹*Department of Astronomy, School of Science, SOKENDAI (The Graduate University for Advanced Studies), 2-21-1 Osawa, Mitaka, Tokyo 181-8588, Japan*

¹²*Laboratory for Multiwavelength Astrophysics, School of Physics and Astronomy, Rochester Institute of Technology, 84 Lomb Memorial Drive, Rochester, NY 14623, USA*

¹³*Department of Earth and Space Sciences, Chalmers University of Technology, Onsala Space Observatory, SE-43992 Onsala, Sweden*

¹⁴*Faculty of Global Interdisciplinary Science and Innovation, Shizuoka University, 836 Ohya, Suruga-ku, Shizuoka 422-8529, Japan*

¹⁵*Instituto Nacional de Astrofísica, Óptica y Electrónica, Tonantzintla, Puebla, México*

¹⁶*Institute of Astronomy, University of Cambridge, Cambridge, CB3 0HA, UK*

¹⁷*Facultad de Astronomía y Geofísica, Universidad de La Plata, La Plata, Argentina*

(Received 20, Dec, 2024; Accepted TBD)

Submitted to ApJ

ABSTRACT

We investigate the dust mass build-up and star formation efficiency of two galaxies at $z > 12$, GHZ2 and GS-z14-0, by combining ALMA and JWST observations with an analytical model that assumes dust at thermal equilibrium. We obtained 3σ constraints on dust mass of $\log M_{\text{dust}}/M_{\odot} < 5.0$ and < 5.3 , respectively. These constraints are in tension with a high dust condensation efficiency in stellar ejecta but are consistent with models with a short metal accretion timescale at $z > 12$. Given the young stellar ages of these galaxies ($t_{\text{age}} \sim 10$ Myrs), dust grain growth via accretion may still be ineffective at this stage, though it likely works efficiently to produce significant dust in galaxies at $z \sim 7$. The star formation efficiencies, defined as the SFR divided by molecular gas mass, reach $\sim 10 \text{ Gyr}^{-1}$ in a 10 Myr timescale, aligning with the expected redshift evolution of ‘starburst’ galaxies with efficiencies that are ~ 0.5 –1 dex higher than those in main-sequence galaxies. This starburst phase seems to be common in UV-bright galaxies at $z > 12$ and is likely associated with the unique conditions of the early phases of galaxy formation, such as bursty star formation and/or negligible feedback from super-Eddington accretion. Direct observations of molecular gas tracers like [C II] will be crucial to further understanding the nature of bright galaxies at $z > 12$.

Keywords: galaxies: evolution - galaxies: formation - galaxies: high-redshift

1. INTRODUCTION

Dust and gas are fundamental components of the interstellar medium (ISM). Gas is the primary fuel for star formation and dust plays a key role in rapidly cooling this component to facilitate the collapse of gas clouds into stars. Cosmic dust originates from stellar phenomena, such as the ejecta of asymptotic giant branch (AGB) stars and rapidly cooling SN ejecta (Dwek & Scalo 1980; Todini & Ferrara 2001; Nozawa et al. 2007). The dust produced by stellar activity (“stellar dust”) grows in the dense ISM through metal accretion and condensation into dust grains (“ISM dust”, e.g., Draine 1990, 2009; Inoue 2011; Zhukovska 2014). Therefore, the dust content within galaxies is directly connected to the star formation history and the metal enrichment process.

The formation and growth of interstellar dust have been studied in relation to other galactic properties, such as the stellar mass, gas mass, and metallicity (Ciesla et al. 2014; Santini et al. 2014; da Cunha et al. 2015; Mancini et al. 2015). The dust-to-gas mass ratio (D/G) represents the fraction of dust relative to the ISM, serving as a powerful tool for investigating dust growth. In the local Universe, D/G has been intensively investigated over the past decades (e.g., Koornneef 1982; Issa et al. 1990; Hirashita et al. 2002; Bendo et al. 2010; Magrini et al. 2011) and found to be correlated with metallicity across a large dynamical range (Lisenfeld & Ferrara 1998; Draine et al. 2007; Leroy et al. 2011; Rémy-Ruyer et al. 2014), which may reflect both chemical evolution and dust grain growth (Dwek 1998; Galliano et al. 2008; Asano et al. 2013; Popping et al. 2017; Graziani et al. 2020). Constraining D/G at high redshift is especially important, as the Universe’s young age limits the contribution of several prominent dust production processes (e.g., Magdis et al. 2012; Popping et al. 2023; Valentino et al. 2024; Palla et al. 2024; Ferrara et al. 2024a).

Recent Atacama Large Millimeter/submillimeter Array (ALMA) studies found a substantial amount of dust at $z = 6\text{--}8$ (Laporte et al. 2017; Tamura et al. 2019; Inami et al. 2022; Witstok et al. 2023a). Several scenarios have been considered to account for this significant dust mass at this early epoch, such as high dust condensation efficiency or efficient metal accretion into ISM (Li et al. 2019; Liu & Hirashita 2019; Graziani et al. 2020; Dayal et al. 2022; Witstok et al. 2023b; Burgarella et al. 2024). Investigation of the emergence of dust in more distant galaxies is essential for understanding the rapid increase in dust mass in the early Universe and identifying the main processes that contribute to this growth (e.g., Burgarella et al. 2024). The small age of the universe further helps explore the rapid pathways that drive dust growth.

Beyond relative dust and gas content, the total gas mass also provides valuable insights, as stars form from cold gas via various cooling mechanisms including dust thermal emission. Specifically, the star formation efficiency (SFE), defined as the star formation rate (SFR) divided by the total (or cold) gas mass, indicates how galaxies convert gas into stars (see Tacconi et al. 2020, for review). Observations of cold gas tracers such as CO and [C II] lines have shown that galaxies on the star-forming main sequence (MS) typically exhibit lower SFE than ‘starburst’ galaxies (e.g., Sanders et al. 1991; Sargent et al. 2012; Tacconi et al. 2018). For instance, Dessauges-Zavadsky et al. (2020) reported a weak redshift evolution of the gas-depletion timescale ($t_{\text{dep}} \propto 1/\text{SFE}$) in $z \sim 5$ UV-selected galaxies, suggesting moderate star formation activity even at high- z . However, whether this weak evolution is maintained at $z > 12$ is entirely unknown, but it could be a key probe to investigate the origin of the overabundance of UV-bright galaxies at $z > 12$ (e.g., Castellano et al. 2022; Atek et al. 2023; Harikane et al. 2023; Finkelstein et al. 2024).

In this paper, we examine the interstellar medium of two $z > 12$ galaxies using ultra-deep ALMA observations of the [O III] emission and the dust continuum. Our study focuses on two of the highest-redshift galaxies known to date, GHZ2 at $z = 12.3$ (Castellano et al. 2024; Zavala et al. 2024a) and GS-z14-0 at $z = 14.2$ (Carniani et al. 2024a). Leveraging the gas phase and stellar metallicities as well as stellar assembly histories observed at $z > 12$, which have been available thanks to the exceptional sensitivity of the *James Webb Space Telescope* (JWST), we aim to explore dust production, dust growth, and star formation efficiency in these early galaxies by exploiting the available deep ALMA observations.

The paper is organized as follows: Section 2 provides an overview of the datasets used in this work. Section 3 describes the method of dust mass measurements. In Section 4, we present our constraints and discussions from the M_* - M_{dust} relations and the gas-phase metallicity Z and dust-to-gas mass relation at $z > 12$, the dust production history and the star formation efficiency of the target galaxies. The conclusions are presented in Section 5. Throughout this paper, we assume a flat universe with the cosmological parameters of $\Omega_{\text{M}} = 0.3$, $\Omega_{\Lambda} = 0.7$, $\sigma_8 = 0.8$, and $H_0 = 70 \text{ km s}^{-1} \text{ Mpc}^{-1}$.

2. TARGETS

2.1. GHZ2

GHZ2 was originally discovered by JWST photometry as part of the GLASS-JWST Program (Treu et al. 2022) and identified in several studies as a robust candidate of the brightest galaxy at $z > 11$ (Castellano et al. 2022; Naidu et al. 2022; Harikane et al. 2023; Bouwens et al. 2023). Its spectroscopic redshift was confirmed to be $z = 12.3$ thanks to the detection of rest-

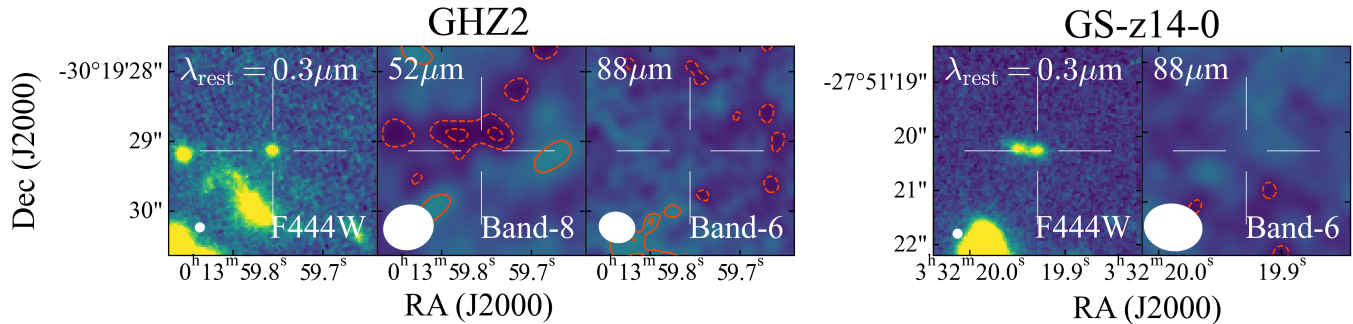


Figure 1. JWST NIRCcam F444W and ALMA Band-6/8 thumbnails of GHZ2 in the rest-frame $0.3\ \mu\text{m}$, $52\ \mu\text{m}$ and $88\ \mu\text{m}$ continuum (left) and GS-z14-0 in the rest-frame $0.3\ \mu\text{m}$ and $88\ \mu\text{m}$ continuum (right). Contour levels are shown in every 2σ from $\pm 3\sigma$. At the positions of the detection in $\lambda_{\text{rest}} = 0.3\ \mu\text{m}$, the dust continuum remains undetected for both galaxies.

frame UV/optical emission line with JWST/NIRSpec (Castellano et al. 2024) and JWST/MIRI (Zavala et al. 2024a). More recently, Zavala et al. (2024b) reported a detection of [O III] $88\ \mu\text{m}$ at $\sim 5\sigma$ level and provided more accurate redshift ($z = 12.3327 \pm 0.0005$). Both NIRSpec and MIRI constrained its metallicity to be low ($Z_{\text{gas}}/Z_{\odot} \sim 0.1$, see also Calabro et al. 2024) and, across this paper, we will adopt the reported value of $Z_{\text{gas}}/Z_{\odot} = 0.05^{+0.12}_{-0.03}$ from Zavala et al. (2024a). The inferred stellar mass changes depending on the SED fitting code and associated assumptions, with a range of $\log M_* [M_{\odot}] = 8.3\text{--}8.9$ (see Appendix in Zavala et al. 2024a) after lens magnification correction of $\mu = 1.3^1$ (Bergamini et al. 2023). Throughout this paper, we will adopt the star-formation history derived by BAGPIPES (Carnall et al. 2018) with a total stellar mass of $\log M_* [M_{\odot}] = 8.27^{+0.23}_{-0.18}$ owing to its non-parametric approach and good agreement with PROSPECTOR (Johnson et al. 2021) results in Harikane et al. (2024, see Figure 4). Note that despite the rich dataset it is still unclear whether an active galactic nucleus (AGN) contributes to the UV emission of GHZ2 (see also, Calabro et al. 2024). And while Zavala et al. (2024b) concluded that this galaxy is likely dominated by star formation activity based on the [O III] $88\ \mu\text{m}$ line width and $H\beta$ line luminosity, further observations are necessary to accurately constrain the stellar mass and potential AGN activity in GHZ2.

2.2. GS-z14-0

GS-z14-0 was identified in the JADES NIRCcam dataset (Robertson et al. 2024) and spectroscopically confirmed via a significant detection of the Ly- α break with NIRSpec/PRISM (Carniani et al. 2024a). Recent ALMA observations reported successful [O III] $88\ \mu\text{m}$ detection at $\sim 6.6\sigma$ (Carniani et al. 2024b; Schouws et al.

2024) and confirmed to be $z = 14.1796 \pm 0.0007$. We will refer to the star formation history with a stellar mass of $\log M_* [M_{\odot}] = 8.84^{+0.09}_{-0.10}$ (after magnification correction; $\mu = 1.17$) and the stellar/gas metallicity of $Z/Z_{\odot} = 0.18^{+0.01}_{-0.01}$ from the PROSPECTOR fitting in Carniani et al. (2024b), which is consistent with the metallicity derived in Schouws et al. (2024).

3. DATA AND ANALYSIS

3.1. ALMA data

ALMA observations of GHZ2 were obtained in both Band-6 and Band-8 by two DDT programs (2021.A.00020.S; PI: Bakx and 2023.A.00017.S; PI: Zavala), where the spectral setups were designed to cover the [O III] $88\ \mu\text{m}$ and the [O III] $52\ \mu\text{m}$ lines, respectively. GS-z14-0 has also been observed by ALMA as part of a DDT program (2023.A.00037.S; PI: Schouws) targeting [O III] $88\ \mu\text{m}$ emission line in Band-6. The calibration of the ALMA data is described in detail in Zavala et al. (2024b, see also, Bakx et al. 2023; Carniani et al. 2024b), here we briefly summarize it. The data were calibrated following standard ALMA pipeline workflow using CASA version 6.5.1 (CASA Team et al. 2022). After removing channels $\pm 300\ \text{km s}^{-1}$ around the detected [O III] $88\ \mu\text{m}$ and expected [O III] $52\ \mu\text{m}$ line frequencies, we created continuum images with a natural weighting to maximize the signal-to-noise ratio. We simply used a dirty image without a primary beam correction because the S/Ns of our target lines are not expected to be high enough to require CLEANING procedure and we require uniform noise distribution within a field of view. The achieved r.m.s levels for GHZ2 and GS-z14-0 data are $3.4\ \mu\text{Jy beam}^{-1}$ and $5.0\ \mu\text{Jy beam}^{-1}$ with beamsizes of $0''.51 \times 0''.43$ and $0''.82 \times 0''.66$ in Band-6 before lens magnification correction, respectively. For GHZ2, the Band-8 observations have an r.m.s depth of $54.6\ \mu\text{Jy beam}^{-1}$ with a beamsize of $0''.71 \times 0''.63$, which is much shallower than Band-6 depth and less constraining on M_{dust} even when taking T_{dust} variation into account.

Figure 1 shows thumbnails in the rest-frame $0.3\ \mu\text{m}$ and $88\ \mu\text{m}$ (and $52\ \mu\text{m}$ for GHZ2) taken by JWST and

¹ While the gravitational lens magnification factor might be up to $\mu \sim 1.6$ due to the closest galaxy at $z = 1.678$, we adopt $\mu = 1.3$ throughout this paper following Zavala et al. (2024b).

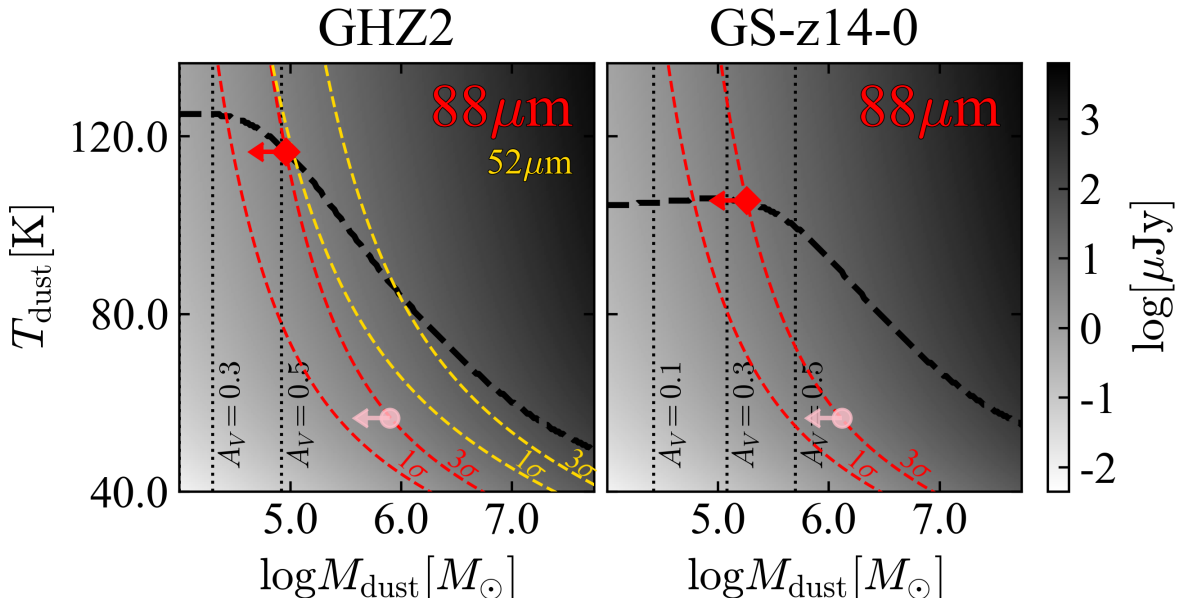


Figure 2. Dust mass and temperatures, color-coded by the signal-to-noise ratio of the dust continuum that is expected at the rest-frame $88\ \mu\text{m}$ for GHZ2 (left) and GS-z14-0 (right). Red solid lines indicate 1σ and 3σ upper limits at the rest-frame $88\ \mu\text{m}$ by assuming a modified black body spectrum after lens magnification correction. The yellow lines on the left panel show upper limits from the rest-frame $52\ \mu\text{m}$ which provides a much less stringent constraint than those derived from the rest-frame $88\ \mu\text{m}$. The acceptable parameter sets and derived dust extinction obtained by the I20 model with the clumpy dust geometry are overlaid in black dashed lines and dotted lines, respectively. Our constraints based on I20 model are shown in red diamonds in the cross-section of 3σ red solid lines and black dashed lines. We also illustrated the 3σ upper limit under the assumption of $T_{\text{dust}} = 50\ \text{K}$ in the pink circles to just demonstrate how I20 model gives tight constraints. Note also that these dust mass constraints do not agree with the observed A_V values (contrary to the values inferred using the I20 model).

ALMA. None of the dust continua were detected even with $\gtrsim 7$ hours on source integrations.

3.2. M_{dust} measurement

We constrain the dust mass of these galaxies by applying an analytical model from Inoue et al. (2020, hereafter I20) to the deep ALMA observations. I20 proposed an algorithm to determine the dust mass (M_{dust}) and temperatures (T_{dust}) under the assumption of radiative equilibrium. In their model, the dust temperature relates to the input radiation source from young stars and cosmic microwave background (CMB) that are absorbed by dust. Then, by incorporating dust geometry, we can calculate the escape probability of UV photons from interstellar media, which results in observable UV luminosities. Among the three available models for the dust geometry provided in I20 (see also, Imara et al. 2018), we specifically employed the ‘‘clumpy’’ geometry as it is considered a reliable approximation for high- z galaxies (e.g., Fudamoto et al. 2023; Kohandel et al. 2023). Indeed, this ‘‘clumpy’’ geometry provided looser constraints on M_{dust} than other geometries in I20, i.e., ‘‘spherical’’ or ‘‘shell’’ under the same assumptions, and therefore our analysis is considered to be conservative. We assumed the dust to be optically thin with an emissivity index of $\beta_{\text{dust}} = 2.0$ (Casey 2012; da Cunha et al. 2021), a

mass absorption coefficient of $\kappa_{\text{UV}} = 5.0 \times 10^4\ \text{cm}^2\ \text{g}^{-1}$, dust emissivity of $\kappa_0 = 30\ \text{cm}^2\ \text{g}^{-1}$ at $100\ \mu\text{m}$, and a clumpiness parameter of $\log \xi_{\text{cl}} = -1.0$ following I20 and Fudamoto et al. (2023). The only input from the observations, beyond the continuum flux density, is the spatial extent of dust. Here, we adopt the spatial extent of the stars traced by the NIRCcam photometry as those of the dust emitting regions ($r_{e,\text{dust}} = r_{e,\text{UV}}$, see Table 1). Note that in the case of GHZ2, if we use the effective radius of $r_{e,\text{UV}} = 39 \pm 10\ \text{pc}$ from Ono et al. (2023) instead of $105 \pm 9\ \text{pc}$, the M_{dust} and M_{gas} constraints become tighter than the fiducial values owing to higher T_{dust} and smaller M_{dyn} , respectively. Hence, the results presented here are considered to be conservative.

In Figure 2, we show the resulting T_{dust} and M_{dust} parameter sets acceptable in our calculations based on the I20 model, with observational constraints corrected for the gravitational magnification ($\mu = 1.3$ and $\mu = 1.17$ for GHZ2 and GS-z14-0, respectively). The upper limits on M_{dust} are shown at the intersection between the analytical predictions (thick black dashed line) and the observational limits (red dashed line). Our calculations support very high T_{dust} ($> 90\ \text{K}$) due to the compact distribution and strong UV radiation. A similar high T_{dust} was also inferred for a $z \sim 10$ galaxy based on recent ALMA observations (Yoon et al. 2023). Metal-

Table 1. Physical parameters of two $z > 12$ galaxies

	GHZ2	GS-z14-0	ref
$M_{\text{UV}}[\text{mag}]$	-20.53 ± 0.01	-20.81 ± 0.16	(1,2)
μ	1.3^\ddagger	1.17	(1,2)
$r_{e,\text{F200W}}[\text{pc}]$	105 ± 9	260 ± 20	(3,2)
$\log M_*[\text{M}_\odot]$	$8.27^{+0.23}_{-0.18}$	$8.84^{+0.09}_{-0.10}$	(4,2)
$\log M_{\text{dyn}}[\text{M}_\odot]$	8.9 ± 0.2	9.0 ± 0.2	(5,2)
$\text{SFR}_{10\text{Myr}}[\text{M}_\odot \text{yr}^{-1}]$	$8.7^{+1.4}_{-1.9}$	$9.9^{+2.3}_{-2.7}$	(4,6)
$\text{SFR}_{100\text{Myr}}[\text{M}_\odot \text{yr}^{-1}]$	$1.4^{+2.0}_{-0.3}$	$5.6^{+1.2}_{-1.3}$	(4,6)
$S_{88\mu\text{m}}[\mu\text{Jy beam}^{-1}]^\ddagger$	< 10.3 (3.4)	< 14.9 (5.0)	(7)
$S_{52\mu\text{m}}[\mu\text{Jy beam}^{-1}]^\ddagger$	< 163.9 (54.6)	-	(7)
$\log M_{\text{dust}}[\text{M}_\odot]^\P$	< 5.0	< 5.3	(7)

NOTE—Every parameter except for the ALMA observational constraints is corrected for magnification shown in the second row.

‡ As described in Zavala et al. (2024a), the magnification for GHZ2 might be ~ 1.6 if we take into account the closest galaxy at $z = 1.682$.

‡ 3σ upper limits with 1σ uncertainties, without correcting the magnification

¶ 3σ upper limits on the dust masses assuming thermal equilibrium model in I20.

1. Castellano et al. (2024), 2. Carniani et al. (2024a), 3. Yang et al. (2022), 4. Zavala et al. (2024a), 5. Zavala et al. (2024b), 6. Carniani et al. (2024b), 7. This work

poor ISM conditions in the target galaxies may also contribute to these elevated dust temperatures (Tamura et al. 2019; Bakx et al. 2020; Sommovigo et al. 2022a; Mitsuhashi et al. 2024). As a consequence of the high dust temperature conditions, our fitting set a tight 3σ upper limits on the dust masses of $\log M_{\text{dust}}/M_\odot < 5.0$ and < 5.3 for GHZ2 and GS-z14-0, respectively. These upper limits agree well with the expected dust extinction ($A_V \lesssim 0.5$ mag) under the ‘clumpy’ dust geometry in each M_{dust} calculated through the escaped/intrinsic UV radiation. In addition, the mass constraints are in good agreement with those obtained by Ferrara et al. (2024b), where they adopt the SED-based extinction as a proxy of the dust mass.

4. RESULTS AND DISCUSSION

4.1. Dust production and evolution at cosmic dawn

In the left panel of Figure 3, we compare our constraints on the dust mass and stellar mass relation with previous constraints for galaxies at $z = 4-7$ (Bakx et al. 2021; Sommovigo et al. 2022a,b; Witstok et al. 2022; Valentino et al. 2024). Our results indicate a lower dust content in galaxies at $z > 12$ compared to those at $z = 4-7$, a trend that persists when compared with samples from Fudamoto et al. (2023), which were derived using a similar methodology. This conclusion holds even when assuming $T_{\text{dust}} = 50$ K (e.g., Sommovigo et al. 2022a,b; Mitsuhashi et al. 2024), implying a dust mass limit about ~ 1 dex larger than our fiducial value, as

shown in Figure 3. A recent study in Burgarella et al. (2024) suggested a potential decrease of the dust-to-stellar mass ratio at $z > 10$, which is in line with our conclusion.

The dust-to-stellar mass ratio (M_{dust}/M_*) is likely influenced by grain growth within the ISM, which is driven by the condensation of metals in dense gas and is thus inversely proportional to gas-phase metallicity (e.g., de Bressan et al. 2014; Burgarella et al. 2024). Given the positive correlation between stellar mass and gas-phase metallicity (i.e., the mass-metallicity relation), grain growth becomes effective around stellar masses of $\log M_*/M_\odot \gtrsim 8.5$ (Mancini et al. 2015). Models that assume very efficient grain growth due to enhanced gas condensation do not align closely with the non-detection of dust continua at $z > 12$ (Popping et al. 2017; Vijayan et al. 2019).

In the left panel of Figure 3, we also plot several (semi-)analytical models of dust production at $z > 6$ (Popping et al. 2017; Imara et al. 2018; Vijayan et al. 2019; Mauerhofer & Dayal 2023; Di Cesare et al. 2023), which predict dust content evolution due to production by stars, destruction by SNe, and grain growth in clouds. These models reproduce observed trends and scatter well at $z = 4-7$, though most seem to overestimate our measurements at $z > 12$, potentially because their models focus on galaxies at $z \sim 7-9$.

Another possible reason for low dust content at $z > 12$ is that dust is expelled or lifted off by the radiation-driven outflows (Ferrara 2024; Ferrara et al. 2024a). In their model, the super-Eddington star formation occurs with significant radiation pressure. In this case, the total dust mass might be underestimated because such expelled dust is no longer in equilibrium. Indeed, GHZ2 is derived to have specific SFR of $\log \text{sSFR} \sim 1.67$ Gyr, which exceeds a critical sSFR ($\log \text{sSFR} \sim 1.4$ Gyr) presented in Ferrara (2024). While GS-z14-0 is expected to have $\log \text{sSFR} \sim 1.3$ Gyr within recent ~ 100 Myr based on its SFH, such a radiation-driven outflow may play an important role for non-detections of the dust continuum.

In the right panel of Figure 3, we explore the relationship between gas-phase metallicity (Z_{gas}) and D/G. The constraints on D/G at low metallicity values are critical to disentangle dust growth scenarios. Here, we computed the gas mass by subtracting the magnification-corrected stellar mass from the dynamical mass ($M_{\text{gas}} = M_{\text{dyn}} - M_*$) assuming negligible dark matter contribution within galaxy centers ($\lesssim r_e$). For GHZ2 and GS-z14-0, the resulting gas masses in our fiducial calculation are $M_{\text{gas}} = 5.8^{+3.7}_{-3.7} \times 10^8 M_\odot$ and $M_{\text{gas}} = 2.6^{+5.2}_{-2.6} \times 10^8 M_\odot$, respectively.

It is worth noting that, the mass of the ionized gas component (M_{ion}) has an insignificant contribution. Based on $L_{\text{H}\beta} - M_{\text{ion}}$ relation presented in Chávez et al. (2014), GHZ2 has $M_{\text{ion}} = 2.5 \times 10^6 - 9.8 \times 10^7 M_\odot$ from the $\text{H}\beta$ flux of $F_{\text{H}\beta} = 0.9 \pm 0.2 \times 10^{-18} \text{ erg s}^{-1} \text{ cm}^{-2}$ and

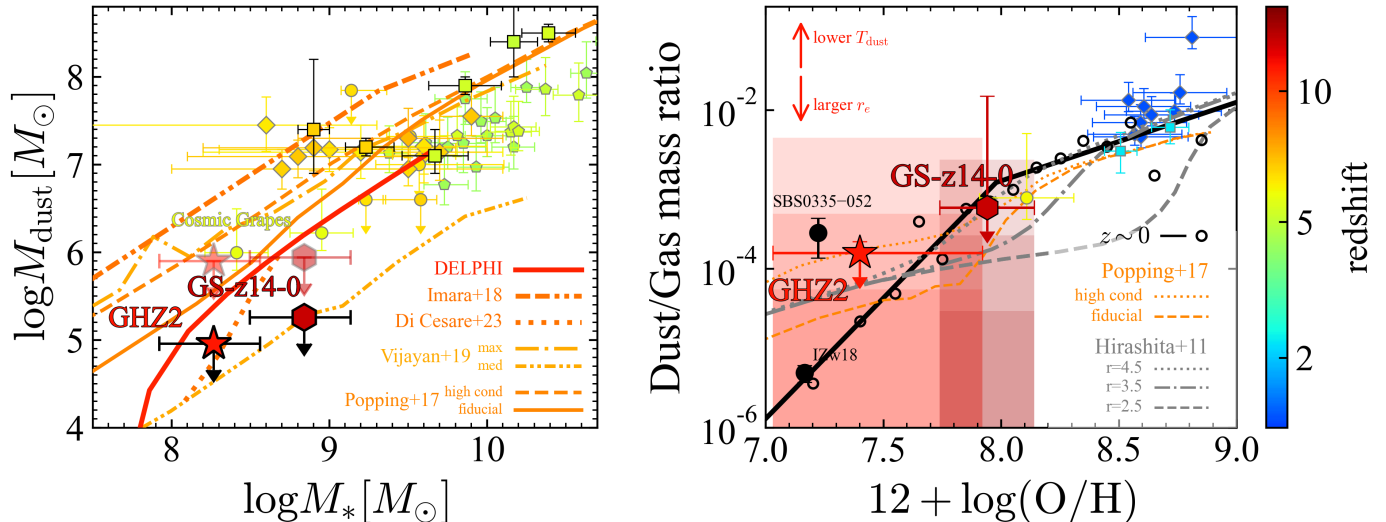


Figure 3. (left) Dust mass as a function of the stellar mass. Our constraints for the galaxies at $z > 12$ along with the previous constraints at $z = 4-8$ (Bakx et al. 2021; Sommovigo et al. 2022a,b; Witstok et al. 2022; Fudamoto et al. 2023; Valentino et al. 2024) and (semi-)analytical models (Popping et al. 2017; Imara et al. 2018; Vijayan et al. 2019; Di Cesare et al. 2023) including DELPHI model (Mauerhofer & Dayal 2023) are shown in colors corresponding to their redshift. For Popping et al. (2017) and Vijayan et al. (2019) models, predictions with different dust condensation efficiencies are shown in different line styles. The markers surrounded by black lines are constraints using the I20 model, whereas those surrounded by gray lines show results by assuming a modified black body radiation with a typical dust temperature (i.e. $T_{\text{dust}} = 50$ K). (right) Dust-to-gas mass ratio against the gas-phase metallicity. Our fiducial constraints from $M_{\text{gas}} = M_{\text{dyn}} - M_*$ are shown in a red star and brown hexagon, and those from $M_{\text{gas}} = 0.1, 0.5, \text{ and } 0.9 (M_{\text{gas}} + M_*)$ are illustrated in red and brown shaded regions with different levels of opacity. Observational constraints at $z = 2-6$ (Magdis et al. 2012; Popping et al. 2023; Valentino et al. 2024) and a model (Popping et al. 2017) are shown in colors depending on their redshift. The black solid line and circles indicated median relation and observations at $z = 0$ (Rémy-Ruyer et al. 2014). The gray lines show models with the power law in the dust size distribution of $r = 4.5$ (dotted), 3.5 (dash-dotted), and 2.5 (dashed), respectively, from Hirashita & Kuo (2011).

electron density of $n_e = 100 - 4000 \text{ cm}^{-3}$ (Zavala et al. 2024a). GS-z14-0 is expected to have $M_{\text{ion}} = 3.0 \times 10^5 - 1.2 \times 10^7 M_{\odot}$ from $F_{\text{H}\beta} = 7.9^{+0.17}_{-0.18} \times 10^{-19} \text{ erg s}^{-1} \text{ cm}^{-2}$ (Helton et al. 2024), assuming of the same range of electron density as GHZ2. We adopt $M_{\text{ion}} = 1.2 \times 10^7 M_{\odot}$ as the lower limit of M_{gas} for GS-z14-0, as $M_{\text{gas}} = M_{\text{dyn}} - M_* = 0$ is unphysical.

We obtained constraints of $\text{D/G} \lesssim 10^{-4}$ at $Z \sim 0.1 Z_{\odot}$ and $\text{D/G} \lesssim 10^{-3}$ at $Z \sim 0.2 Z_{\odot}$. As described in Popping et al. (2017), the D/G ratio as a function of metallicity is determined by the balance of the condensation efficiency (f_{cond}) and accretion timescales (τ_{acc}) since both condensation and accretion promote the increase of the D/G. Among their calculations, models with high f_{cond} do not align well even in the extreme case with 100% condensation and no accretion (‘no-acc’ model, although their calculations are up to $z \sim 9$). At the metallicity range of $Z < 0.5 Z_{\odot}$, their fiducial model follows the fixed accretion timescale $\tau_{\text{acc}} = 100 \text{ Myr}$ (‘fix-tau’ model), which is consistent with our constraints. As a consequence, the inferred upper limits favor a moderate f_{cond} rather than the high-efficiency model in Popping et al. (2017).

In the right panel of Figure 3, we compare our target galaxies with local dwarf galaxies, SBS0335-052 and

IZw 18 (Schneider et al. 2016). These two galaxies show a dramatic difference in D/G at similar gas-phase metallicity. Schneider et al. (2016) found that ISM density causes this variety because of the efficient grain growth in high-density ISM. Further investigation on the ISM density, such as the molecular gas density (or electron density as a proxy), might be helpful to confirm the potential inefficient dust grain growth of galaxies at $z > 12$.

As Liu & Hirashita (2019) suggested, both high f_{cond} and short τ_{acc} can account for large dust amounts in massive galaxies at $z \sim 7$ (Hashimoto et al. 2019; Tamura et al. 2019; Bakx et al. 2020). In their results, the high f_{cond} model predicts large dust mass at the very early stage of the galaxy formation ($\lesssim 10 \text{ Myr}$) while the short τ_{acc} model imply a rapid increase of dust mass at the age of $\sim 100 \text{ Myr}$. If our target galaxies at $z > 12$ are progenitors of these $z \sim 7$ massive galaxies, our results support the short τ_{acc} model with $\tau_{\text{acc}} \sim 5-100 \text{ Myr}$, while the high f_{cond} model is unsupported. From another perspective, the models by Hirashita & Kuo (2011) reveal that dust size distribution and τ_{acc} significantly affect D/G at metallicities of $Z \sim 0.1-2 Z_{\odot}$ (see also, Asano et al. 2013). Our results at $Z \sim 0.2 Z_{\odot}$, while having a large uncertainty, suggest that a moderately large-size dust distribution with $\tau_{\text{acc}} \sim 10 \text{ Myr}$ can con-

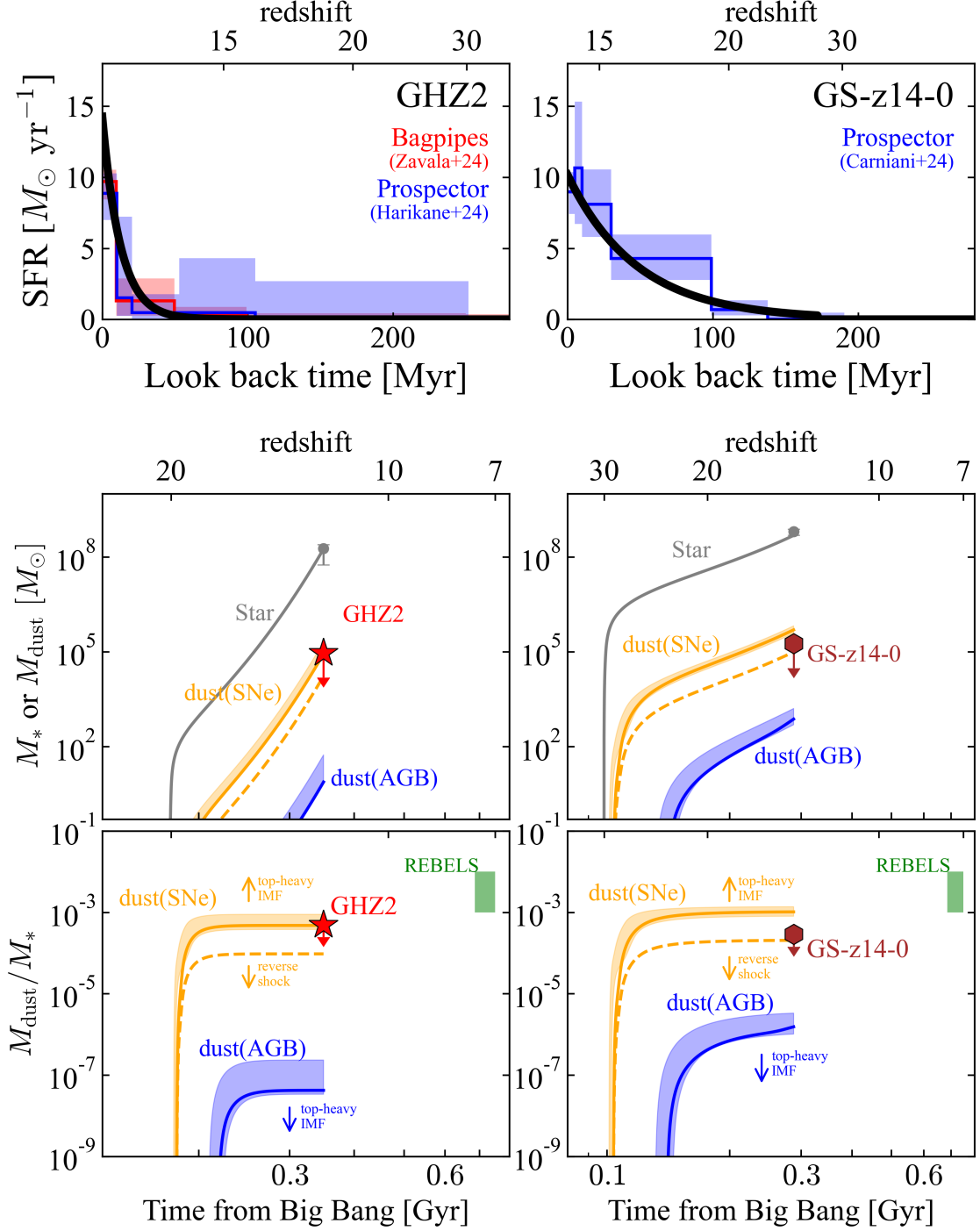


Figure 4. Dust and star formation history derived from non-parametric SFH and SN/AGB dust yield models for GHZs (left) and GS-z14-0 (right). (top) Smoothed exponentially rising star formation history (black) derived from BAGPIPES (red, Zavala et al. 2024a) and PROSPECTOR (blue, Carniani et al. 2024b; Harikane et al. 2024). (middle, bottom) Our constraints on the dust mass with the previous results from the REBELS survey (Topping et al. 2022; Dayal et al. 2022; Ferrara et al. 2022). The models of the dust production history from SFH are based on Valiante et al. (2009) with the SN dust yield from Bianchi & Schneider (2007) and Zhukovska et al. (2008), and the AGB dust yield from Ferrarotti & Gail (2006) and ATON code (Dell’Agli et al. 2019). For Zhukovska et al. (2008) and ATON models, we show ranges with 10^{-4} – $0.1 Z_{\odot}$ with orange and blue shaded regions. The effect of the initial mass function (IMF) and reverse shock is shown in two arrows. The SN yield by Bianchi & Schneider (2007) model with 20% dust survival fraction is shown in the orange dashed line.

sistently explain the low D/G observed at low metallicities, as shown in Figure 3.

Here, we emphasize the importance of the direct observations of molecular gas tracers. In the right panel of Figure 3, we also illustrate the acceptable D/Gs based on M_{gas} assuming gas mass fractions of $f_{\text{gas}} = M_{\text{gas}}/(M_{\text{gas}} + M_*) = 0.1, 0.5, \text{ and } 0.9$ instead of those from $M_{\text{dyn}} - M_*$. Nevertheless, it is impossible to disentangle any models with this broad f_{gas} range of 0.1–0.9. Further ALMA observations targeting [C II] or CO lines will be a key to directly constrain f_{gas} and confirm the gas mass from the dynamical masses. For instance, [C II] line can be detected in 3–15 hours source integration in case of $f_{\text{gas}} \sim 0.9$ based on the calibration of $L_{[\text{C II}]} / M_{\text{mol}}$ in Zanella et al. (2018)².

In addition to grain growth, dust destruction can play a critical role, particularly by SN reverse shocks. Figure 4 shows the evolution of stellar and dust masses from supernovae (SNe) and asymptotic giant branch (AGB) stars, based on each galaxy’s SFH derived using BAGPIPES or PROSPECTOR (Zavala et al. 2024a; Carniani et al. 2024b; Harikane et al. 2024, see also section 2). The SFHs are parameterized with an exponential profile ($\text{SFR}(t) \propto \exp(t/\tau)$), with star formation starting at $z = 20$ for GHZ2 and $z = 30$ for GS-z14-0. Our predictions are based on a recipe presented in Valiante et al. (2009, see also, Schneider & Maiolino (2024) for recent review) with the SN dust yield from Bianchi & Schneider (2007) and Zhukovska et al. (2008), and the AGB dust yield from Ferrarotti & Gail (2006) and the ATON code (Dell’Agli et al. 2019). Given the metal-poor nature of the galaxies at $z > 12$, we use the dust yield model with the metallicity of 10^{-4} – $0.1 Z_{\odot}$. We integrate the dust yield from stars ranging 0.1 – $100 M_{\odot}$ under a Larson (Larson 1998) IMF with $\alpha = 1.35$ and $M_{\text{ch}} = 0.35$, which is similar to a Salpeter IMF (Salpeter 1955).

Given the young stellar ages derived from SED fitting ($\lesssim 150$ Myr) and the age of the universe at these redshifts ($\lesssim 300$ Myr), dust from SNe dominates the bulk mass. For GS-z14-0, a high $> 80\%$ destruction efficiency by SN reverse shocks is necessary to reproduce the observed dust-to-stellar mass ratios, while destruction is not necessarily significant for GHZ2 (see Figure 4). The surviving dust mass fraction of $< (100 - 80) = 20\%$ in case of GS-z14-0 is actually consistent with theoretical studies (e.g., Nozawa et al. 2007; Biscaro & Cherchneff 2016; Kirchschrager et al. 2019). The expected significant dust destruction in GS-z14-0 by SN reverse shock contrasts with that inferred for dust-rich galaxies

at $z \sim 7$ (Leńiewska & Michałowski 2019). While inefficient dust destruction or high condensation efficiency may play a more important role in these lower redshift galaxies (Dayal et al. 2022, see also, Palla et al. 2024), it is also possible that the large dust content in REBELS galaxies may be the result of efficient ISM grain growth given their longer ages of tens to hundreds of Myr compared to our $z > 12$ systems.

We also found that a lower dust survival rate is necessary to explain the upper limits if the IMF is more top-heavy. Specifically, $\lesssim 4\%$ dust survival rate is required in GS-z14-0 under $M_{\text{ch}} = 10$ instead of $M_{\text{ch}} = 0.35$ in the Larson IMF (comparable to the top-heavy IMF), which is smaller than the expectations from several models (e.g., Marassi et al. 2015). Although some theoretical models predict a much lower dust survival rate (e.g., Nozawa et al. 2007; Slavin et al. 2020), it may suggest that the top-heavy IMF scenario is not preferred to explain the overabundance of UV-bright galaxies at $z > 10$ from their low dust contents.

4.2. Star formation efficiency

In this section, we compare efficiencies of gas consumption at $z > 12$ with those at $z < 9$. In our fiducial calculations, the total gas masses of the target galaxies are computed as $M_{\text{gas}} = M_{\text{dyn}} - M_*$ as outlined in section 4.1 and, following Aravena et al. (2024), we assume the ISM is dominated by the molecular gas ($M_{\text{gas}} \simeq M_{\text{mol}}$). As in section 4.1, we also calculate gas masses assuming $f_{\text{gas}} = 0.1$ – 0.9 . The caveats associated with these assumptions will be discussed below. On the other hand, we calculate the SFRs by averaging the non-parametric SFHs over timescales of 10 Myr and 100 Myr (Table 1).

Figure 5 illustrates the evolution of the star formation efficiency (SFE), defined as $\text{SFR}/M_{\text{mol}}$. For comparison, we plotted data from main-sequence (MS) and ‘starburst’ (SB) galaxies from PHIBSS (Tacconi et al. 2018), lensed DSFGs (Aravena et al. 2016; Jarugula et al. 2021; Zavala et al. 2022), unlensed DSFGs (Birkin et al. 2021), ALPINE (Dessauges-Zavadsky et al. 2020) and REBELS (Aravena et al. 2024). We also show the scaling relations from Tacconi et al. (2020) and Scoville et al. (2017) at the stellar mass of $M_* = 10^{10} M_{\odot}$. While the range of stellar masses at each redshift spreads $\log M_*/M_{\odot} = 8$ – 11 (with high redshift galaxies showing systematically smaller stellar masses), the dependence of the SFE on the stellar mass is small ($\propto 1/10^{0.01-0.03}$). Also, it is worth noting that molecular gas tracers differ across studies (CO in PHIBSS and SMGs, [C II] in ALPINE and REBELS), but these variations do not introduce systematic uncertainties with the dynamical mass-based estimations (Dessauges-Zavadsky et al. 2020; Birkin et al. 2021; Aravena et al. 2024).

For GHZ2, the SFR averaged over 100 Myr, $\text{SFR}_{100 \text{ Myr}}$, is smaller than $\text{SFR}_{10 \text{ Myr}}$, owing to its inferred rapidly increasing star formation activity (see Fig-

² The calibration in Zanella et al. (2018) do not cover the metallicity range of $Z \lesssim 0.2 Z_{\odot}$ (see also, Rémy-Ruyer et al. 2014). The estimation of [C II] line luminosity here may be optimistic as [C II] line is likely to be fainter in low- Z galaxies (e.g., Hashimoto et al. 2019; Harikane et al. 2020; Bakx et al. 2024)

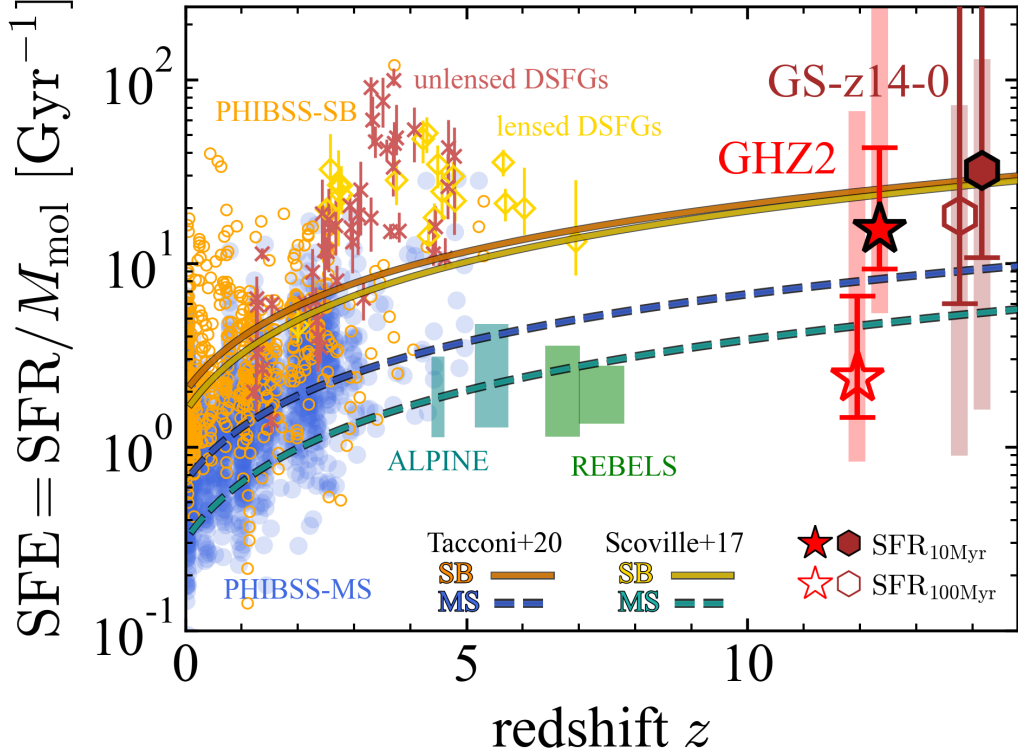


Figure 5. Redshift evolution of the star formation efficiency. Our fiducial calculations (red stars and brown hexagons) are shown based on $\text{SFR}_{10\text{Myr}}$ (filled) and $\text{SFR}_{100\text{Myr}}$ (open markers), respectively. We also illustrate SFEs based on the gas masses assuming $f_{\text{gas}} = 0.1\text{--}0.9$ in red and brown shaded regions associated with each marker. Shifts have been added in the x-axis direction for ease of viewing. Previous studies of the MS galaxies from PHIBSS (blue circles, Tacconi et al. 2018), ALPINE (blue shades, Dessauges-Zavadsky et al. 2020), and REBELS (green shades, Aravena et al. 2024) as well as SB galaxies from PHIBSS (orange circles), unlensed DSFGs (brown crosses, Birkin et al. 2021), lensed DSFGs (yellow diamonds, Aravena et al. 2016; Jarugula et al. 2021; Zavala et al. 2022) are also plotted. The predicted evolution in Tacconi et al. (2020, orange solid and blue dashed lines) and Scoville et al. (2017, yellow solid and green dashed lines).

ure 4). The $\text{SFR}_{100\text{Myr}}$ of GHZ2 is consistent with the expected evolution of MS galaxies, but the most recent star-forming episode, represented by $\text{SFR}_{10\text{Myr}}$ shows a higher efficiency in better agreement with the so-called “starbursts” systems. In contrast, GS-z14-0 has a comparable high SFE at both 10 Myr and 100 Myr timescales (given its more smoothly-rising SFH), indicating a relatively longer-term starburst mode. The SFEs of GHZ2 and GS-z14-0 in 10 Myr timescale are $\text{SFH}_{10\text{Myr}} \gtrsim 10 \text{Gyr}^{-1}$ and are in a good agreement with the expected redshift evolution of starburst galaxies. This contrasts with the UV-bright galaxies at $z = 4\text{--}8$ selected via the Lyman break method, which has SFEs of $\sim 1 \text{Gyr}^{-1}$ and follows the MS scaling relation or even prefers a shallower evolution (Dessauges-Zavadsky et al. 2020; Aravena et al. 2024). Indeed, this high SFE in GHZ2 is in line with the interpretation in Zavala et al. (2024b), H II galaxy-like nature of GHZ2.

The timescales over which the star formation is being calculated can be important when comparing our measurements with those at lower redshifts. In Figure

5, the SFRs of UV-selected galaxies at $z = 4\text{--}8$ (i.e., ALPINE/REBELS galaxies) are calculated from rest-frame UV and IR continuum tracing the average star formation activity within ~ 100 Myr. Indeed, Endsley et al. (2024) reported that around 10% of $z \approx 6\text{--}9$ UV-bright galaxies with $M_{\text{UV}} \sim -20$ mag show an order of magnitude higher SFR in < 10 Myr. Therefore, $\sim 10\%$ of the ALPINE/REBELS galaxies may have an order of magnitude larger SFR within a < 10 Myr timescale, implying a higher SFR in better agreement with the SB scaling relation.³ On the other hand, as described

³ A fraction of galaxies having rising SFHs may increase in galaxies with the small absolute UV magnitude (Endsley et al. 2024; Asada et al. 2024; Harikane et al. 2024). As the ALPINE and REBELS galaxies have smaller absolute UV magnitude ($M_{\text{UV}} \sim -21\text{--}22$ mag) than those at Endsley et al. (2024, $M_{\text{UV}} \sim -20$ mag), the fraction of the galaxies lying on the SB sequence in 10 Myr timescale may be higher than $\sim 10\%$ in the ALPINE and REBELS galaxies. However, at least not every galaxy has like that rising SFHs (Topping et al. 2022; Palla et al. 2024).

above, both GHZ2 and GS-z14-0 are likely under a starburst episode, which may suggest that this ‘starburst’ phase with efficient gas consumption is more ubiquitous among UV-bright galaxies at $z > 12$ than at $z \sim 6$.

As described in Carniani et al. (2024b), GS-z14-0 exhibits a smaller gas fraction ($M_{\text{gas}}/(M_* + M_{\text{gas}}) \sim 0.3$) than those at $z = 4-8$ ($M_{\text{gas}}/M_* \sim 1$ Dessauges-Zavadsky et al. 2020; Aravena et al. 2024), indicating small gas reservoir compared with an existing stellar mass. Approximating $M_{\text{gas}} \approx f_b M_{\text{halo}}$, where f_b and M_{halo} is the cosmic baryon fraction and the host halo mass, respectively, the stellar-to-halo mass ratio ($\epsilon_* = M_*/M_{\text{halo}}$) becomes around 0.5, which is consistent with recent studies implying high ϵ_* (e.g., Casey et al. 2024; Shuntov et al. 2024). The high SFE and small gas fraction in GS-z14-0 align also with the feedback-free star formation model (Dekel et al. 2023; Li et al. 2024). All these scenarios might be (at least partially) responsible for the reported overabundance of UV-bright galaxies at $z \gtrsim 10$. We thus hypothesize that GS-z14-0 is converting most of its molecular gas into stars in a recent ‘starburst’, and will run out the molecular gas (or expel the gas and dust components, see Ferrara 2024), and turn off their star formation within the next several 10 Myrs.

On the other hand, GHZ2 shows a large fraction of molecular gas mass within the baryonic content ($M_{\text{gas}}/(M_* + M_{\text{gas}}) \sim 0.7$). Its instantaneous high SFE and high gas fraction may be the result of a bursty star formation history, which increases the visibility of UV-bright galaxies during short and intense bursts of star formation (e.g., Sun et al. 2023; Kravtsov & Belokurov 2024). Further observations capturing rest-frame optical stellar continuum will enable us to make more accurate constraints on the stellar mass, and therefore on the gas fraction.

One major caveat in using $M_{\text{dyn}} - M_*$ as a proxy of M_{gas} is the uncertain fraction of the molecular gas within the total gas. However, if the molecular gas fraction is below unity, the derived M_{mol} decreases, and the SFE increases. Therefore, the adopted molecular gas fraction does not affect our conclusion. We acknowledge, however, that conducting direct observations of cold ISM tracers, such as [C II] or CO lines, is crucial to put better constraints on the molecular gas mass. As shown in the shaded boxes in Figure 5, the assumption of the f_{gas} range of 0.1–0.9 prevents imposing any meaningful constraints on the SFE. The detection experiment of [C II] will be an important key to confirm or rule out our conclusion.

5. SUMMARY

In this paper, we have investigated the dust and gas content of the brightest galaxies at $z > 12$, GHZ2, and GS-z14-0, based on direct ALMA observations that trace the bulk of the dust mass in these galaxies. From the combination of ultra-deep ALMA observations and an analytical thermal equilibrium model, we have found:

- The 3σ upper limits on the dust continuum at $\lambda_{\text{rest}} = 88 \mu\text{m}$ are $10.3 \mu\text{Jy}$ and $14.9 \mu\text{Jy}$ for Band-6 observations on GHZ2 and GS-z14-0, respectively. Combining these observations with an analytical model based on thermal equilibrium and clumpy dust geometry (Inoue et al. 2020), we derived dust mass upper limits of $\log M_{\text{dust}}/M_{\odot} < 5.0$ and < 5.3 , respectively.
- The comparison of our constraints on $M_* - M_{\text{dust}}$ plane and dust production models at $z > 4$ do not imply efficient dust grain growth with extreme condensation efficiency f_{cond} . Assuming most massive galaxies at $z > 12$ are potential progenitors of most massive galaxies at $z = 7$, a short accretion timescale scenario is supported rather than a high f_{cond} scenario in Liu & Hirashita (2019). Initial dust size distributions with a moderate amount of large-size grains, resulting in $\tau_{\text{acc}} \sim 10$ Myr, are preferred in our constraints on the Z–D/G relation.
- Given the very young ages of the target galaxies, dust yield from AGB stars and grain growth are not likely to be effective. The observed dust-to-stellar mass ratios in GS-z14-0 can be naturally explained by the dust survival rate of $< 20\%$ from the reverse shocks by SN.
- Based on the gas masses from $M_{\text{gas}} = M_{\text{dyn}} - M_*$ and SFHs, we inferred star formation efficiencies within the past 10 Myr, which reach high values above $\sim 10 \text{Gyr}^{-1}$, comparable with the predicted SFEs’ evolution of starburst galaxies. GHZ2 may exhibit short starburst-like episodes only for relatively short periods of up to ~ 10 Myr, while GS-z14-0 is likely to have such starburst mode in a relatively long term of ~ 100 Myr. From a comparison with UV-bright galaxies at $z \sim 6$, we hypothesize that such ‘starburst’ activity may be more ubiquitous in UV-bright galaxies at $z > 12$ than at $z \sim 6$, potentially due to bursty SFHs (e.g., Sun et al. 2023) and/or negligible feedback coming from super-Eddington star formation (e.g., Dekel et al. 2023).

Our study demonstrates the importance of observing cold interstellar medium tracers, such as dust continuum and [C II] line observations with ALMA to derive the current and future star formation activity of UV-bright galaxies. Since our analysis with the thermal equilibrium model predicts very high T_{dust} , further deep ALMA observations at high frequency to capture near the peak of dust thermal emission will be useful to identify dust at $z > 12$. For instance, ~ 30 hours ALMA Band 9 observations covering rest-frame $\sim 30 \mu\text{m}$ allows us to add tighter constraint on M_{dust} at $T_{\text{dust}} > 100 \text{K}$ regime. To further understand the emergence of dust across the

Universe, investigating the gas and dust content of most massive galaxies at $z \sim 8-11$ is necessary to constrain the grain growth in the ISM. Systematic comparison of ISM conditions, such as gas/electron density, across the Universe, might be critical to understanding the origin of the lack of dust and the potential ‘starburst’ nature of $z > 12$ galaxies.

ACKNOWLEDGMENTS

We thank P. Dayal for providing us with data from their semi-analytical calculation. This paper makes use of the following ALMA data: ADS/JAO.ALMA#2021.A.00020.S, #2023.A.00017, #2023.A.00037. ALMA is a partnership of ESO (representing its member states), NSF (USA), and NINS (Japan), together with NRC (Canada), MOST and ASIAA (Taiwan), and KASI (Republic of Korea), in cooperation with the Republic of Chile. The Joint ALMA Observatory is operated by ESO, AUI/NRAO, and NAOJ. IM and AKI acknowledge support from NAOJ ALMA Scientific Research Grant number 2020-16B. The authors acknowledge the GLASS and JADES teams led by Tommaso Treu and Daniel Eisenstein & Nora Luetzgendorf, respectively, for developing their observing programs. The *JWST* data presented in this article were obtained from the Mikulski Archive for Space Telescopes (MAST) at the Space Telescope Science Institute. The specific observations analyzed can be found in the MAST [10.17909/wz7w-2208](https://archive.stsci.edu/10.17909/wz7w-2208). Data analysis was in part carried out using the Multi-wavelength Data Analysis System operated by the Astronomy Data Center (ADC), National Astronomical Observatory of Japan. KK acknowledges support from the Knut and Alice Wallenberg Foundation (KAW 2020.0081). PS acknowledges INAF Mini Grant 2022 ”The evolution of passive galaxies through cosmic time”.

REFERENCES

- Aravena, M., Spilker, J. S., Bethermin, M., et al. 2016, *MNRAS*, 457, 4406
- Aravena, M., Heintz, K., Dessauges-Zavadsky, M., et al. 2024, *A&A*, 682, A24
- Asada, Y., Sawicki, M., Abraham, R., et al. 2024, *MNRAS*, 527, 11372
- Asano, R. S., Takeuchi, T. T., Hirashita, H., & Inoue, A. K. 2013, *Earth, Planets and Space*, 65, 213
- Atek, H., Shuntov, M., Furtak, L. J., et al. 2023, *MNRAS*, 519, 1201
- Bakx, T. J. L. C., Tamura, Y., Hashimoto, T., et al. 2020, *MNRAS*, 493, 4294
- Bakx, T. J. L. C., Sommovigo, L., Carniani, S., et al. 2021, *MNRAS*, 508, L58
- Bakx, T. J. L. C., Zavala, J. A., Mitsuhashi, I., et al. 2023, *MNRAS*, 519, 5076
- Bakx, T. J. L. C., Algera, H. S. B., Venemans, B., et al. 2024, *MNRAS*, 532, 2270
- Bendo, G. J., Wilson, C. D., Warren, B. E., et al. 2010, *MNRAS*, 402, 1409
- Bergamini, P., Acebron, A., Grillo, C., et al. 2023, *ApJ*, 952, 84
- Bianchi, S., & Schneider, R. 2007, *MNRAS*, 378, 973
- Birkin, J. E., Weiss, A., Wardlow, J. L., et al. 2021, *MNRAS*, 501, 3926
- Biscaro, C., & Cherchneff, I. 2016, *A&A*, 589, A132
- Bouwens, R., Illingworth, G., Oesch, P., et al. 2023, *MNRAS*, 523, 1009
- Burgarella, D., Buat, V., Theulé, P., et al. 2024, *arXiv e-prints*, arXiv:2410.23959
- Calabro, A., Castellano, M., Zavala, J. A., et al. 2024, *arXiv e-prints*, arXiv:2403.12683
- Carnall, A. C., McLure, R. J., Dunlop, J. S., & Davé, R. 2018, *MNRAS*, 480, 4379
- Carniani, S., Hainline, K., D'Eugenio, F., et al. 2024a, *Nature*, 633, 318
- Carniani, S., D'Eugenio, F., Ji, X., et al. 2024b, *arXiv e-prints*, arXiv:2409.20533
- CASA Team, Bean, B., Bhatnagar, S., et al. 2022, *PASP*, 134, 114501
- Casey, C. M. 2012, *MNRAS*, 425, 3094
- Casey, C. M., Akins, H. B., Shuntov, M., et al. 2024, *ApJ*, 965, 98
- Castellano, M., Fontana, A., Treu, T., et al. 2022, *ApJL*, 938, L15
- Castellano, M., Napolitano, L., Fontana, A., et al. 2024, *ApJ*, 972, 143
- Chávez, R., Terlevich, R., Terlevich, E., et al. 2014, *MNRAS*, 442, 3565
- Ciesla, L., Boquien, M., Boselli, A., et al. 2014, *A&A*, 565, A128
- da Cunha, E., Walter, F., Smail, I. R., et al. 2015, *ApJ*, 806, 110
- da Cunha, E., Hodge, J. A., Casey, C. M., et al. 2021, *ApJ*, 919, 30
- Dayal, P., Ferrara, A., Sommovigo, L., et al. 2022, *MNRAS*, 512, 989
- de Bennassuti, M., Schneider, R., Valiante, R., & Salvadori, S. 2014, *MNRAS*, 445, 3039
- Dekel, A., Sarkar, K. C., Birnboim, Y., Mandelker, N., & Li, Z. 2023, *MNRAS*, 523, 3201
- Dell'Agli, F., Valiante, R., Kamath, D., Ventura, P., & García-Hernández, D. A. 2019, *MNRAS*, 486, 4738
- Dessauges-Zavadsky, M., Ginolfi, M., Pozzi, F., et al. 2020, *A&A*, 643, A5
- Di Cesare, C., Graziani, L., Schneider, R., et al. 2023, *MNRAS*, 519, 4632
- Draine, B. T. 1990, in *Astronomical Society of the Pacific Conference Series*, Vol. 12, *The Evolution of the Interstellar Medium*, ed. L. Blitz, 193–205
- Draine, B. T. 2009, in *Astronomical Society of the Pacific Conference Series*, Vol. 414, *Cosmic Dust - Near and Far*, ed. T. Henning, E. Grün, & J. Steinacker, 453
- Draine, B. T., Dale, D. A., Bendo, G., et al. 2007, *ApJ*, 663, 866
- Dwek, E. 1998, *ApJ*, 501, 643
- Dwek, E., & Scalo, J. M. 1980, *ApJ*, 239, 193
- Endsley, R., Stark, D. P., Whitler, L., et al. 2024, *MNRAS*, 533, 1111
- Ferrara, A. 2024, *A&A*, 684, A207
- Ferrara, A., Carniani, S., di Mascia, F., et al. 2024a, *arXiv e-prints*, arXiv:2409.17223
- Ferrara, A., Pallottini, A., & Sommovigo, L. 2024b, *arXiv e-prints*, arXiv:2410.19042
- Ferrara, A., Sommovigo, L., Dayal, P., et al. 2022, *MNRAS*, 512, 58
- Ferrarotti, A. S., & Gail, H. P. 2006, *A&A*, 447, 553
- Finkelstein, S. L., Leung, G. C. K., Bagley, M. B., et al. 2024, *ApJL*, 969, L2
- Fudamoto, Y., Inoue, A. K., & Sugahara, Y. 2023, *MNRAS*, 521, 2962
- Galliano, F., Dwek, E., & Chianial, P. 2008, *ApJ*, 672, 214
- Graziani, L., Schneider, R., Ginolfi, M., et al. 2020, *MNRAS*, 494, 1071
- Harikane, Y., Ouchi, M., Inoue, A. K., et al. 2020, *ApJ*, 896, 93
- Harikane, Y., Ouchi, M., Oguri, M., et al. 2023, *ApJS*, 265, 5

- Harikane, Y., Inoue, A. K., Ellis, R. S., et al. 2024, arXiv e-prints, arXiv:2406.18352
- Hashimoto, T., Inoue, A. K., Mawatari, K., et al. 2019, PASJ, 71, 71
- Helton, J. M., Rieke, G. H., Alberts, S., et al. 2024, arXiv e-prints, arXiv:2405.18462
- Hirashita, H., & Kuo, T.-M. 2011, MNRAS, 416, 1340
- Hirashita, H., Tajiri, Y. Y., & Kamaya, H. 2002, A&A, 388, 439
- Imara, N., Loeb, A., Johnson, B. D., Conroy, C., & Behroozi, P. 2018, ApJ, 854, 36
- Inami, H., Algera, H. S. B., Schouws, S., et al. 2022, MNRAS, 515, 3126
- Inoue, A. K. 2011, Earth, Planets and Space, 63, 1027
- Inoue, A. K., Hashimoto, T., Chihara, H., & Koike, C. 2020, MNRAS, 495, 1577
- Issa, M. R., MacLaren, I., & Wolfendale, A. W. 1990, A&A, 236, 237
- Jarugula, S., Vieira, J. D., Weiss, A., et al. 2021, ApJ, 921, 97
- Johnson, B. D., Leja, J., Conroy, C., & Speagle, J. S. 2021, ApJS, 254, 22
- Kirchschlager, F., Schmidt, F. D., Barlow, M. J., et al. 2019, MNRAS, 489, 4465
- Kohandel, M., Ferrara, A., Pallottini, A., et al. 2023, MNRAS, 520, L16
- Koornneef, J. 1982, A&A, 107, 247
- Kravtsov, A., & Belokurov, V. 2024, arXiv e-prints, arXiv:2405.04578
- Laporte, N., Ellis, R. S., Boone, F., et al. 2017, ApJL, 837, L21
- Larson, R. B. 1998, MNRAS, 301, 569
- Leroy, A. K., Bolatto, A., Gordon, K., et al. 2011, ApJ, 737, 12
- Leńniewska, A., & Michałowski, M. J. 2019, A&A, 624, L13
- Li, Q., Narayanan, D., & Davé, R. 2019, MNRAS, 490, 1425
- Li, Z., Dekel, A., Sarkar, K. C., et al. 2024, A&A, 690, A108
- Lisenfeld, U., & Ferrara, A. 1998, ApJ, 496, 145
- Liu, H.-M., & Hirashita, H. 2019, MNRAS, 490, 540
- Magdis, G. E., Daddi, E., Béthermin, M., et al. 2012, ApJ, 760, 6
- Magrini, L., Bianchi, S., Corbelli, E., et al. 2011, A&A, 535, A13
- Mancini, M., Schneider, R., Graziani, L., et al. 2015, MNRAS, 451, L70
- Marassi, S., Schneider, R., Limongi, M., et al. 2015, MNRAS, 454, 4250
- Mauerhofer, V., & Dayal, P. 2023, MNRAS, 526, 2196
- Mitsuhashi, I., Harikane, Y., Bauer, F. E., et al. 2024, ApJ, 971, 161
- Naidu, R. P., Oesch, P. A., van Dokkum, P., et al. 2022, ApJL, 940, L14
- Nozawa, T., Kozasa, T., Habe, A., et al. 2007, ApJ, 666, 955
- Ono, Y., Harikane, Y., Ouchi, M., et al. 2023, ApJ, 951, 72
- Palla, M., De Looze, I., Relaño, M., et al. 2024, MNRAS, 528, 2407
- Popping, G., Somerville, R. S., & Galametz, M. 2017, MNRAS, 471, 3152
- Popping, G., Shivaiei, I., Sanders, R. L., et al. 2023, A&A, 670, A138
- Rémy-Ruyer, A., Madden, S. C., Galliano, F., et al. 2014, A&A, 563, A31
- Robertson, B., Johnson, B. D., Tacchella, S., et al. 2024, ApJ, 970, 31
- Salpeter, E. E. 1955, ApJ, 121, 161
- Sanders, D. B., Scoville, N. Z., & Soifer, B. T. 1991, ApJ, 370, 158
- Santini, P., Maiolino, R., Magnelli, B., et al. 2014, A&A, 562, A30
- Sargent, M. T., Béthermin, M., Daddi, E., & Elbaz, D. 2012, ApJL, 747, L31
- Schneider, R., Hunt, L., & Valiante, R. 2016, MNRAS, 457, 1842
- Schneider, R., & Maiolino, R. 2024, A&A Rv, 32, 2
- Schouws, S., Bouwens, R. J., Ormerod, K., et al. 2024, arXiv e-prints, arXiv:2409.20549
- Scoville, N., Lee, N., Vanden Bout, P., et al. 2017, ApJ, 837, 150
- Shuntov, M., Ilbert, O., Toft, S., et al. 2024, arXiv e-prints, arXiv:2410.08290
- Slavin, J. D., Dwek, E., Mac Low, M.-M., & Hill, A. S. 2020, ApJ, 902, 135
- Sommovigo, L., Ferrara, A., Pallottini, A., et al. 2022a, MNRAS, 513, 3122
- Sommovigo, L., Ferrara, A., Carniani, S., et al. 2022b, MNRAS, 517, 5930
- Sun, G., Faucher-Giguère, C.-A., Hayward, C. C., et al. 2023, ApJL, 955, L35
- Tacconi, L. J., Genzel, R., & Sternberg, A. 2020, ARA&A, 58, 157
- Tacconi, L. J., Genzel, R., Saintonge, A., et al. 2018, ApJ, 853, 179
- Tamura, Y., Mawatari, K., Hashimoto, T., et al. 2019, ApJ, 874, 27
- Todini, P., & Ferrara, A. 2001, MNRAS, 325, 726
- Topping, M. W., Stark, D. P., Endsley, R., et al. 2022, MNRAS, 516, 975
- Treu, T., Roberts-Borsani, G., Bradac, M., et al. 2022, ApJ, 935, 110

- Valentino, F., Fujimoto, S., Giménez-Arteaga, C., et al. 2024, *A&A*, 685, A138
- Valiante, R., Schneider, R., Bianchi, S., & Andersen, A. C. 2009, *MNRAS*, 397, 1661
- Vijayan, A. P., Clay, S. J., Thomas, P. A., et al. 2019, *MNRAS*, 489, 4072
- Witstok, J., Jones, G. C., Maiolino, R., Smit, R., & Schneider, R. 2023a, *MNRAS*, 523, 3119
- Witstok, J., Smit, R., Maiolino, R., et al. 2022, *MNRAS*, 515, 1751
- Witstok, J., Shivaee, I., Smit, R., et al. 2023b, *Nature*, 621, 267
- Yang, L., Morishita, T., Leethochawalit, N., et al. 2022, *ApJL*, 938, L17
- Yoon, I., Carilli, C. L., Fujimoto, S., et al. 2023, *ApJ*, 950, 61
- Zanella, A., Daddi, E., Magdis, G., et al. 2018, *MNRAS*, 481, 1976
- Zavala, J. A., Casey, C. M., Spilker, J., et al. 2022, *ApJ*, 933, 242
- Zavala, J. A., Castellano, M., Akins, H. B., et al. 2024a, *Nature Astronomy*
- Zavala, J. A., Bakx, T., Mitsuhashi, I., et al. 2024b, *arXiv e-prints*, arXiv:2411.03593
- Zhukovska, S. 2014, *A&A*, 562, A76
- Zhukovska, S., Gail, H. P., & Trieloff, M. 2008, *A&A*, 479, 453